

Stable topological insulators achieved using high energy electron beams

Lukas Zhao,¹ Marcin Konczykowski,² Haiming Deng,¹ Inna Korzhovska,¹
 Milan Begliarbekov,¹ Zhiyi Chen,¹ Evangelos Papalazarou,³ Marino Marsi,³
 Luca Perfetti,² Andrzej Hruban,⁴ Agnieszka Wołoś,^{5,6} & Lia Krusin-Elbaum¹

¹*Department of Physics, The City College of New York, CUNY, New York, NY 10031, USA*

²*Laboratoire des Solides Irradiés, École Polytechnique, CNRS,
 CEA, Université Paris-Saclay, 91128 Palaiseau cedex, France*

³*Laboratoire de Physique des Solides, CNRS,
 Université Paris-Saclay, Université Paris-Sud, 91405 Orsay, France*

⁴*Institute of Electronic Materials Technology, 01-919 Warsaw, Poland*

⁵*Institute of Physics, Polish Academy of Sciences, 02-668 Warsaw, Poland and*

⁶*Faculty of Physics, University of Warsaw, 00-681 Warsaw, Poland*

Topological insulators are transformative quantum solids with immune-to-disorder metallic surface states having Dirac band structure. Ubiquitous charged bulk defects, however, pull the Fermi energy into the bulk bands, denying access to surface charge transport. Here we demonstrate that irradiation with swift (~ 2.5 MeV energy) electron beams allows to compensate these defects, bring the Fermi level back into the bulk gap, and reach the charge neutrality point (CNP). Controlling the beam fluence we tune bulk conductivity from p - (hole-like) to n -type (electron-like), crossing the Dirac point and back, while preserving the Dirac energy dispersion. The CNP conductance has a two-dimensional (2D) character on the order of ten conductance quanta $G_0 = e^2/h$, and reveals, both in Bi_2Te_3 and Bi_2Se_3 , the presence of only two quantum channels corresponding to two topological surfaces. The intrinsic quantum transport of the topological states is accessible disregarding the bulk size.

Unconventional quantum matter can be easily hidden within the rich existing library of condensed matter and to recognize it often novel concepts have to be invoked. It also takes a profound understanding of the real material constraints that can prevent the unconventional properties from being detected. Three-dimensional (3D) topological insulators are a spectacular example of this¹ – narrow-band semiconductors, well known for their high performance as thermoelectrics,² they were discovered to support unusual gapless robust two-dimensional (2D) surface states that are fully spin-polarized with Dirac-type linear electronic energy-momentum dispersion^{3,4}, which makes them protected against backscattering by disorder^{3–6}. These materials have narrow bulk gaps ($\sim 200 - 300$ meV) and have charge carriers donated by intrinsic crystalline lattice defects such as vacancies and antisites⁷. As a result, the conduction through the bulk and its intermixing with surface channels is what largely denies direct access to surface charge transport required for the implementation in spin-based nanoelectronics⁸ or fault-tolerant topological quantum computing⁴.

Extensive attempts to reduce the contribution of bulk carriers, involving techniques such as nanostructured synthesis/growth^{9,10}, chemical doping¹¹ or compositional tuning¹², have relied on electrostatic gating of micro- or nano-structures comprising tens of nanometer thin films¹³ or similarly thin exfoliated crystals¹⁴ to gain less ambiguous access to the surface states. Here we demonstrate that bulk conductivity in topological insulators (TIs) can be decreased by orders of magnitude to charge neutrality point on a large (depth) scale by the controlled use of electron beams which for energies below ~ 3 MeV are known to produce a well-defined, stable and uniform spread of Frenkel (vacancy-interstitial) pairs¹⁵ within their penetration range of hundreds of microns. The combined effect of these pairs is to compensate for the intrinsic charged defects responsible for the conductivity of the bulk while crystal lattice integrity is maintained and, as we demonstrate by angularly resolved photoemission spectroscopy (ARPES), the topological Dirac surface states remain robust. Stable surface conduction channels are achieved when a sufficient irradiation dose is followed by the optimally engineered annealing protocol, thereby resolving one of the key limitations of bulk TIs.

Results

Compensating bulk carriers using electron beams. Under exposure to light particles such as electrons the production of vacancy-interstitial point defects¹⁶ in solids known as Frenkel pairs is well established. The pair formation has an energy threshold which scales with atomic weight – it is high for heavy Bi and is lower for lighter Te and Se, and the effective cross-section σ for pair creation on different sublattices in materials containing these elements depends on the projectile energy (Figs. 1a,b and Supplementary Figs. 1,2). This defines a pair-production window: below these thresholds the given sub-lattice becomes immune to

irradiation while at energies above ~ 3 MeV clustering and even nuclear reactions¹⁷ may occur. The process of Frenkel pair formation is straightforward and can be well controlled. The charge is primarily delivered by introduced vacancies, since at room temperature interstitials do not contribute owing to their much lower (compared to vacancies) migration barriers. For electron beams energies above ~ 1.5 MeV the effective cross-section σ on a Bi sublattice is the highest and we will show that donor type defects on this sublattice do prevail. For energies below Bi threshold (~ 1.2 MeV) the creation of Frenkel pairs will be mostly on Se or Te sublattices and, correspondingly, by tuning electron beam energy a different mix of donor/acceptor defects and a net acceptor charge doping can be expected.

Generally, crystal growth of tetradymite crystals such as Bi_2Te_3 and Bi_2Se_3 results in equilibrium defect configurations comprising vacancies and antisites on both sublattices^{7,18}. The net free charge balance that delivers carriers to bulk conduction or valence bands from these defects can be varied by growth conditions or doping¹¹. In undoped Bi_2Se_3 , where Se vacancies are presumed to dominate, the net conduction is by electron carriers or *n*-type. In Bi_2Te_3 , where antisites are prevalent¹⁹ the conductivity is usually *p*-type, namely by hole carriers, although by varying stoichiometry it has been grown of either conductivity type. Without *a priori* knowledge of the net donor or acceptor flavor of the pairs on different sublattices we have chosen first to irradiate *p*-type topological materials Bi_2Te_3 and Ca-doped¹¹ Bi_2Se_3 with 2.5 MeV electron beams which create Frenkel pairs on all sublattices according to $\sigma(E)$, shown in Fig. 1b and Supplementary Fig. 2. Our results demonstrate that in the above mentioned Bi-based TIs at this energy the net flavor is of donor type. It is also important to note that even for relatively high ($\gtrsim 1 \text{ C} \cdot \text{cm}^{-2}$) electron irradiation doses the lattice parameters remain unchanged (see Supplementary Fig. 3).

Ambipolar conduction tuned by irradiation dose. Longitudinal resistivity ρ_{xx} of the initially *p*-type Bi_2Te_3 measured at 20 K *in situ* in the irradiation chamber (see Methods) as a function of irradiation dose is shown in Fig. 1e. Most immediately notable features in the figure are (i) a nearly three orders of magnitude resistivity increase to a maximum ρ_{xx}^{max} and (ii) the observed ambipolar conduction as a function of irradiation dose with well-distinguished *p* (hole) and *n*(electron) conduction regions. The resistivity maximum ρ_{xx}^{max} (the conductivity minimum σ_{xx}^{min}) is at the charge neutrality point where conduction is converted from *p*- to *n*-type, as determined from Hall resistivity (see Fig. 2). The same type conversion is observed in Ca-doped Bi_2Se_3 (Supplementary Fig. 4a and Supplementary Note 1) which is also *p*-type¹¹. As long as the terminal irradiation dose ϕ is relatively low, below $\sim 0.1 \text{ C} \cdot \text{cm}^{-2}$, $\rho_{xx}(\phi)$ traces its shape upon temperature cycling to room temperature and back to 20 K, with ρ_{xx}^{max} reproduced by the next irradiation cycle. Here it is apparent that the value of ϕ_{max} at the

charge neutrality point is not universal; it depends on the starting free carrier concentration n_b but can be straightforwardly scaled using universal slope $\simeq \frac{\partial n_b}{\partial \phi}$ of quasi-linear variation of n_b vs. dose (Fig. 2a and Supplementary Figs. 4b and 5).

Longitudinal and Hall resistivities across CNP. *Ex situ* measured resistivities of Bi_2Te_3 crystals irradiated to different terminal doses and taken to room temperature before the chill-down to 4.2 K are in full correspondence with the *in situ* results. Figure 2a shows three orders of magnitude increase in ρ_{xx} to the maximum, ρ_{xx}^{max} , at $\phi_{\text{max}} \approx 90 \text{ C} \cdot \text{cm}^{-2}$ higher than the *in situ* ϕ_{max} (Fig. 1e) likely owing in part to some defect migration (mostly interstitials¹⁶) above 100 K. The *p*- to *n*-type conversion is clearly seen in Hall resistance R_{xy} (Fig. 2b and Figs. 2f-2h) flipping its slope dR_{xy}/dH and Hall coefficient $R_H = -\frac{1}{n_b e}$ changing sign in the conversion region. Near charge neutrality point (CNP) the net residual bulk carrier density $n_b = n_D - n_A$ is very low (n_D and n_A are concentrations of donors and acceptors respectively). In this region local charge fluctuations can be very large creating inhomogeneity akin to a network of puddle-like *p-n* junctions that nonlinearly screen random potential on long length scales²⁰ and a simple estimate of n_b is no longer appropriate¹⁴. Mobilities in our crystals are significantly higher ($\mu \cong 7,000 - 11,000 \text{ cm}^2\text{V}^{-1}\text{s}^{-1}$, see Supplementary Table 1) than a commonly observed $\lesssim 1,000 \text{ cm}^2\text{V}^{-1}\text{s}^{-1}$ range¹⁴ near the CNP region.

Shubnikov-de Haas oscillations and Berry phase. The change in net carrier density induced by irradiation is reflected in the observed Shubnikov-de Haas (SdH) quantum oscillations (Fig. 2c-2e) of sheet and Hall resistances, ΔR_{xx} and ΔR_{xy} , from which an estimate of the Fermi surface size can be obtained (Supplementary Table 1). The Fermi vector in pristine crystals $k_F \approx 0.025 \text{ \AA}^{-1}$ is consistently larger than after irradiation and, for example, the dose $\phi \cong 89 \text{ C} \cdot \text{cm}^{-2}$ which tunes the crystal close to CNP results in $k_F \approx 0.014 \text{ \AA}^{-1}$. The corresponding net carrier densities are $n_b = 5.06 \times 10^{17} \text{ cm}^{-3}$ and $n_b \simeq 1.08 \times 10^{17} \text{ cm}^{-3}$ respectively. At higher irradiation dose $\phi \cong 99 \text{ C} \cdot \text{cm}^{-2}$, with $k_F \approx 0.022 \text{ \AA}^{-1}$ Fermi surface size becomes comparable to the pristine material. A comparison of these numbers with carrier densities obtained independently from Hall data (Supplementary Table 1) reveals a good agreement between the two techniques near CNP but about an order of magnitude higher estimate of n_b by the latter²¹ well outside the CNP region. Berry phase $\varphi_B = 2\pi\beta$ can be estimated from SdH oscillations using a semiclassical description²² $\Delta R_{xx} = A_{\text{SdH}} \cos[2\pi(\frac{H_F}{H} + \frac{1}{2} + \beta)]$, where A_{SdH} is the oscillation amplitude, H_F is the frequency in $1/H$, and β is the Berry factor. Near CNP the obtained Berry factor is $\beta = 0.5 \pm 0.06$ as expected for the topological Dirac particles, while outside the CNP region a trivial value of $\beta \simeq 0$ is obtained (Fig. 2i).

Nonequilibrium defect compensation at low irradiation dose. The stability of net

carrier density crucially depends on the terminal irradiation dose. First we illustrate that for low terminal electron doses ($\phi \lesssim 0.1 \text{ C} \cdot \text{cm}^{-2}$) the resistivity is not stable as it evolves from the n -region after irradiation through CNP back into the p -region. The experiment was to simply change the dwelling time at room temperature (RT) to allow for vacancies to diffuse. The result is the reverse conversion (Fig. 3a) from metallic-like resistivity on the n -side just after irradiation, through insulating resistivity at CNP (after nearly 250 hours at RT), and back to a weakly semiconducting-like resistivity on the p -side. As the system evolves across CNP a weak antilocalization quantum interference correction²³ to classical magnetoresistance (MR) emerges in the non-equilibrated conversion region (Fig. 3b), with a complex MR structure and nonlinear Hall resistivity (see Supplementary Fig. 6), likely reflecting a presence of two carrier types. From isochronal annealing experiments (Supplementary Fig. 7 and Supplementary Note 2) we estimate energy barriers controlling defect migration to be $\sim 0.8 \text{ eV}$ corresponding to $\sim 9,000 \text{ K}$, in line with literature values for vacancy migration in solids¹⁶. We conclude that at low terminal doses while defect migration is sluggish, the equilibrium is not attained.

Achieving stability at CNP with high irradiation dose. Next we demonstrate that stability can be controlled and optimized in a reverse conversion process by the annealing protocol when the terminal electron dose is sufficiently high. This is the key part of the material modification process by electron irradiation; without it surface transport via electron irradiation could not be obtained²⁴. We demonstrate this for the samples exposed to the dose ten times higher, $\phi = 1 \text{ C} \cdot \text{cm}^{-2}$. Fig. 4a shows temperature dependence of sheet resistance R_{xx} and conductance G_{xx} of Bi_2Te_3 tuned back to CNP through a thermal protocol shown in Fig. 4b, where it remained for months of testing (Supplementary Figs. 8,9 and Supplementary Note 3). As clearly seen in ARPES (Figs. 4c,d and Supplementary Fig. 10), under this annealing protocol Dirac dispersion remains preserved. The effect of tuning conduction from the irradiation induced n -type (Fig. 4c) back toward CNP (Fig. 4d) is a relative shift of the Fermi level toward the Dirac point, consistent with transport data and with the calculated band structure⁵ of Bi_2Te_3 (see cartoons in Figs. 2f-h).

$R_{xx}(T)$ increases exponentially as the temperature decreases, turning below $\sim 200 \text{ K}$ into variable range hopping (Supplementary Fig. 11 and Supplementary Note 4). This bulk behavior is cut off at low temperatures when the contribution from the surfaces becomes comparable and a temperature-independent surface transport with minimum conductance¹⁴ $G_{xx}^{\min} \cong 20 e^2/h$ reveals its quantum nature. The 2D character of this region is witnessed by MR that depends only on the transverse component of magnetic field $H_{\perp} = H \cos \theta$ (Figs. 4e-h). Unlike the quadratic-in-field MR of a conventional metal, the large ($\gtrsim 10\%$) magnetoresistance at CNP (Fig. 4a) is found to be linear in field (Figs. 4f,h).

The topological protection of the surface states near CNP can be tested in at least three ways. One, by breaking time reversal symmetry (TRS) which should gap out Dirac states. Another, by the appearance of topological Berry phase⁴ of π (see Fig. 2i). And yet another, by detecting two-dimensional (2D) weak antilocalization (WAL) of Dirac particles traveling through time reversed paths²³ associated with this Berry phase. Fig. 4a shows that applying TRS-breaking magnetic field indeed causes $R_{xx}(T)$ at the lowest temperatures to upturn, showing localizing behavior consistent with opening of the Dirac gap (see, e.g., ref. [25]). From this we conclude that near CNP, even with the complex Bi_2Te_3 band structure, topological conduction channels dominate.

Stable 2D quantum transport at CNP. As we approach CNP, weak antilocalization (WAL) quantum correction to classical conductivity emerges at low magnetic fields as a characteristic positive magnetoresistance cusp²³ (inset in Fig. 4b). In close proximity to CNP the corresponding cusp in negative magnetoconductance scales with the transverse field $H_{\perp} = H \cos \theta$ (Fig. 4e,g), confirming its 2D character. In this case, the number n_Q of quantum conduction channels contributing to WAL can be estimated from 2D localization theory²⁶

$$\Delta G(B) \simeq \alpha \frac{e^2}{2\pi^2 \hbar} f\left(\frac{B_{\phi}}{B}\right), \quad (1)$$

where $\Delta G(B)$ is the low-field quantum correction to 2D magnetoconductance, coefficient $\alpha = n_Q/2$ equals to 1/2 for a single 2D channel, $f(x) \equiv \ln x - \psi(1/2 + x)$, ψ is the digamma function, and field $B_{\phi} = \frac{\hbar}{4el_{\phi}^2}$ is related to the dephasing length l_{ϕ} of interfering electron paths. In Bi_2Te_3 at CNP the fit (in Fig. 4e) yields $\alpha \simeq 1.26 \pm 0.1$ corresponding to $n_Q \sim 2$, smaller than G_{xx}^{\min} . The obtained value of ~ 2 is quite remarkable since ‘universality’ of n_Q has been questioned²⁷ given a likely formation of subsurface two-dimensional electron gas (2DEG) states of bulk origin. In Bi_2Se_3 , where the Dirac point is expected to coincide with CNP, the fit similarly yields $\alpha \simeq 1.12 \pm 0.1$ (Fig. 4g), corresponding to two 2D quantum channels we associate with two independent topological surfaces.

Finally, we remark that using thermal protocol illustrated in Fig. 4b we found that once CNP is reached the system remains there for months on cycling, which was the duration of our experiments. This robustness suggests that at higher electron doses vacancies are likely correlated; e.g. di-vacancies can form^{16,28} and it is known that point-defect complexes can be stabilized²⁹ in systems with multiple sublattices. With the choice of electron beam energy and terminal electron dose controlling the stability of pairs, and with a suitably designed thermal tuning to charge neutrality, the high-energy electron irradiation offers a path to large scale access to topological states.

Methods

Crystal growth and structural characterization. Single crystals of Bi_2Te_3 , and $\text{Ca}(0.09\%)$ -doped Bi_2Se_3 were grown by the standard Bridgman-Stockbarger method using a vertical temperature gradient pull. X-ray diffraction of crystals was performed in a Panalytical diffractometer using $\text{Cu K}\alpha$ ($\lambda = 1.5405\text{\AA}$) line from Philips high intensity ceramic sealed tube (3 kW) X-ray source with a Soller slit (0.04 rad) incident and diffracted beam optics. Transmission electron microscopy was performed at Evans Analytical Group.

Angularly resolved photoemission spectroscopy (ARPES). ARPES measurements were performed on the FemtoARPES setup³⁰ using a Ti:sapphire laser operated at 0.25 MHz repetition rate. The specimens were probed with the 4th harmonic (at 6.26 eV), with an overall spectral resolution better than 30 meV. The data were taken along Γ - M and Γ - K directions. We found no substantial differences for measurements performed on several cleaved surfaces.

Electron irradiation. Electron irradiations were carried out in NEC Pelletron-type electrostatic accelerator in Laboratoire de Physique des Solides at École Polytechnique, Palaiseau, configured with a low temperature target maintained at ~ 20 K in a chamber filled with liquid hydrogen fed from a close cycle refrigerator. All irradiations were performed with samples kept at 20 K, below the mobility threshold of the interstitials which tend to be more mobile than vacancies¹⁶ – this ensured the stability of all charges introduced by the irradiation process. It also allowed us to evaluate thermal migration of interstitials during the annealing process. The size of the 2.5 MeV electron beam spot was reduced to 5 mm by a circular diaphragm aperture, with uniformity of the beam current ensured with a constant beam sweep in x and y -directions at two non-commensurate frequencies. Careful calibration of the beam current density, typically of $2\text{ }\mu\text{A}$ on a 0.2 cm^2 surface, was performed by periodic introduction of a Faraday cage between the diaphragm and the sample chamber and the measurement of current collected on the control metallic sample. Beam current densities, limited to $10\text{ }\mu\text{C} \cdot \text{cm}^{-2}\text{s}^{-1}$ by the cooling rate, allowed modifications of carrier concentration on the order of 10^{20} cm^{-3} .

Transport measurements. The system was set up for *in situ* transport measurements which could be monitored as a function of electron dose in real time. Crystals used in the irradiation experiments were typically $15\text{ }\mu\text{m}$ thick with spark-weld electrical contacts placed in van der Pauw contact configuration. *Ex situ* transport and Shubnikov-de Haas oscillations measurements were performed in Quantum Design Physical Property Measurement System equipped with 14 T magnet. In *ex situ* measurements, when samples were exfoliated to thicknesses of 200 nm and below, lithographically designed contacts with Ti/Au metallurgy

were used (see Fig. 4a). Annealing experiments up to 200°C (such as shown in Fig. 4b and Supplementary Note 2) were performed in a box furnace in flowing nitrogen.

-
- ¹ Brumfiel, G. Star material. *Nature* **66**, 310 (2010).
 - ² Venkatasubramanian, R., Siivola, E., Colpitts, T. & O’Quinn, B. Thin-film thermoelectric devices with high room-temperature figures of merit. *Nature* **413**, 597–602 (2001).
 - ³ Fu, L., Kane, C. & Mele, E. Topological insulators in three dimensions. *Phys. Rev. Lett.* **98**, 106803 (2007).
 - ⁴ Qi, X.-L. & Zhang, S.-C. Topological insulators and superconductors. *Rev. Mod. Phys.* **83**, 1057–1110 (2011).
 - ⁵ Zhang, H. *et al.* Topological insulators in Bi₂Se₃, Bi₂Te₃, and Sb₂Te₃ with a single Dirac cone on the surface. *Nature Phys.* **5**, 438–442 (2009).
 - ⁶ Hsieh, D. *et al.* A tunable topological insulator in the spin helical Dirac transport regime. *Nature* **460**, 1101–5 (2009).
 - ⁷ Scanlon, D. *et al.* Controlling bulk conductivity in topological insulators: key role of anti-site defects. *Adv. Mater.* **24**, 2154–2158 (2012).
 - ⁸ Yazyev, O., Moore, J. & Louie, S. Spin polarization and transport of surface states in the topological insulators Bi₂Se₃ and Bi₂Te₃ from first principles. *Phys. Rev. Lett.* **105**, 266806 (2010).
 - ⁹ Kong, D. *et al.* Few-layer nanoplates of Bi₂Se₃ and Bi₂Te₃ with highly tunable chemical potential. *Nano Lett.* **10**, 2245 (2010).
 - ¹⁰ Brahlek, M., Koirala, N., Salehi, M., Bansal, N. & Oh, S. Emergence of decoupled surface transport channels in bulk insulating Bi₂Se₃ thin films. *Phys. Rev. Lett.* **113**, 026801 (2014).
 - ¹¹ Checkelsky, J. G. *et al.* Quantum interference in macroscopic crystals of nonmetallic Bi₂Se₃. *Phys. Rev. Lett.* **103**, 246601 (2009).
 - ¹² Zhang, J. *et al.* Band structure engineering in (Bi_{1-x}Sb_x)₂Te₃ ternary topological insulators. *Nature Comm.* **2**, 574 (2011).
 - ¹³ Chen, J. *et al.* Gate-voltage control of chemical potential and weak antilocalization in Bi₂Se₃. *Phys. Rev. Lett.* **105**, 176602 (2010).
 - ¹⁴ Kim, D. *et al.* Surface conduction of topological Dirac electrons in bulk insulating Bi₂Se₃. *Nature Phys.* **8**, 459 (2010).
 - ¹⁵ Bois, P. & Beuneu, F. Defect production in Bi and dilute alloys irradiated by electrons. *J. Phys. F - Metal Phys.* **37**, 6041 (1988).

- ¹⁶ Damask, A. & Dienes, G. *Point defects in metals* (Gordon and Breach, New York, 1963).
- ¹⁷ Petwal, V. C., Senecha, V. K., Subbaiah, K. V., Soni, H. C. & Kotaiah, S. Optimization studies of photo-neutron production in high-Z metallic targets using high energy electron beam for ADS and transmutation. *Pramana-J. Phys.* **68**, 235–241 (2007).
- ¹⁸ Xue, L. *et al.* First-principles study of native point defects in Bi₂Se₃. *AIP Advances* **3**, 052105 (2013).
- ¹⁹ Drašar, C., Lošták, P. & Uher, C. Doping and defect structure of tetradymite-type crystals. *J. Electronic Mat.* **39**, 2162 (2010).
- ²⁰ Skinner, B., Chen, T. & Shklovskii, B. Why is the bulk resistivity of topological insulators so small? *Phys. Rev. Lett.* **109**, 176801 (2012).
- ²¹ Taskin, A. A. & Ando, Y. Quantum oscillations in a topological insulator Bi_{1-x}Sb_x. *Phys. Rev. B* **80**, 085303 (2009).
- ²² Mikitik, G. P. & Sharlai, Y. V. Manifestation of Berry’s phase in metal physics. *Phys. Rev. Lett.* **82**, 2147 (1999).
- ²³ Garate, I. & Glazman, L. Weak localization and antilocalization in topological insulator thin films with coherent bulk-surface coupling. *Phys. Rev. B* **86**, 035422 (2012).
- ²⁴ Rischau, C. W., Leridon, B., Fauque, B., Metayer, V. & van der Beek, C. J. Doping of Bi₂Te₃ using electron irradiation. *Phys. Rev. B* **88**, 205207 (2013).
- ²⁵ Kim, D. J., Xia, J. & Fisk, Z. Topological surface state in the Kondo insulator samarium hexaboride. *Nature Mater.* **13**, 466–470 (2014).
- ²⁶ Hikami, S., Larkin, A. & Nagaoka, Y. Spin-orbit interaction and magnetoresistance in the two-dimensional random system. *Progress Theor. Phys.* **63**, 707–710 (1980).
- ²⁷ Zhang, L. *et al.* Weak localization effects as evidence for bulk quantization in Bi₂Se₃ thin films. *Phys. Rev. B* **88**, 121103(R) (2013).
- ²⁸ Petersen, M. C., Larsen, A. N. & Mesli, A. Divacancy defects in germanium studied using deep-level transient spectroscopy. *Phys. Rev. B* **82**, 075203 (2010).
- ²⁹ Bois, P. & Beuneu, F. Displacement threshold energy in pure Bi and dilute BiTe alloys. *J. Phys. F - Metal Phys.* **17**, 2365 (1987).
- ³⁰ Faure, J. *et al.* Full characterization and optimization of a femtosecond ultraviolet laser source for time and angle-resolved photoemission on solid surfaces. *Rev. Sci. Instrum.* **83**, 043109 (2012).

Acknowledgements We thank Boris Spivak for his insightful comments. We are grateful to Martin Krusin and Vadim Oganessian for the critical reading of the manuscript. This work was supported by the NSF grants DMR-1312483-MWN and DMR-1420634 (L.K.-E.), DOD-W911NF-13-1-0159 (L.K.-E.), ANR-13-IS04-0001-01 (M.K. and L.P.), EMIR project 11-11-0923 (M.K. and L.K.-E.), and NCN grant No. 2011/03/B/ST3/03362 (A.W.). The work of M.M. is supported by Investissements dAvenir LabEx PALM (ANR-10-LABX-0039-PALM).

Author contributions Experiments were designed by L.K.-E. and M.K.. A.H. grew Bi_2Te_3 and Bi_2Se_3 :Ca crystals and A.W. selected pristine crystals with low carrier densities. I.K. performed structural and chemical characterization of all crystals. I. K. and M. B. fabricated exfoliated structures. Transport measurements were performed by L.Z., H.D. and M.K., data analysis was done by L.Z., M.K. and L.K.-E. ARPES measurements were carried out by E.P., L.P. and M.M.. L.K.-E. wrote the manuscript with critical input from L.Z. and M.K.

Additional information The authors declare that they have no competing financial interests. Supplementary information accompanies this paper on www.nature.com. Correspondence and requests for materials should be addressed to L. K.-E.

FIGURE LEGENDS

Figure 1 | Tuning bulk conductivity of topological materials by swift particle irradiation. **a**, Energetic electron beams can penetrate solids to a depth of many tens of microns. Electron irradiation affects the bulk but not the robust topological surfaces. **b**, Impinging electrons induce formation of Frenkel vacancy-interstitial pairs (inset), which act to compensate the intrinsic bulk defects. Main panel: Calculated crosssections σ for Frenkel pair production in Bi, Te and Se sublattices as a function of electron energy E , assuming displacement energy¹⁶ ~ 25 eV. Energy thresholds, E_{th} , in σ are set by atomic weight; choosing $E < E_{th}^{Bi}$ or $E > E_{th}^{Bi}$ allows to tune Fermi level in both p - and n -type TIs. **c**, Transmission electron microscopy image of Bi_2Te_3 with electron dose $\phi = 1 \text{ C}\cdot\text{cm}^{-2}$; the atomic displacements of ~ 1 per 5,000 are not seen. Scale bar is 1 nm. **d**, ARPES spectrum taken at 130 K (see Methods) of a Bi_2Te_3 crystal after irradiation with high electron dose of $1.7 \text{ C}\cdot\text{cm}^{-2}$. The irradiated sample becomes n -type, with Dirac point at $E_{DP} = -290(10)$ meV relative to the Fermi level E_F (just below the bottom of the bulk conduction band). It demonstrates electronic robustness of Dirac spectrum against electron irradiation. **e**, Resistivity of p -type Bi_2Te_3 irradiated with 2.5 MeV electrons *vs.* dose ϕ (red squares) measured *in situ* at 20 K

shows about three orders of magnitude increase at the charge neutrality point (CNP) where the conduction is converted from p - to n -type, moving the Fermi level E_F across the Dirac point (see cartoon). Cycling to room temperature reverses the process, which can be recovered by further irradiation (blue circles) and stabilized. The conversion from n - to p -type is obtained in a material such as Pb-based TI, where vacancies on the Pb sites are known to be of acceptor type.

Figure 2 | Transport and quantum oscillations across charge neutrality point.

a, Top: Longitudinal resistivity ρ_{xx} of Bi_2Te_3 crystals irradiated to different terminal doses and measured at 4.2 K shows three orders of magnitude increase at CNP where the bulk is converted from p - to n -type, as indicated by the sign change of the slope dR_{xy}/dH of Hall resistance R_{xy} shown in **(b)**. Middle: Inverse Hall coefficient $1/eR_H \simeq -n_b$ gives an estimate of net carrier density n_b as a function of dose. At CNP R_H changes sign. Bottom: Mobility just above CNP appears higher than just below, with the expected trend of μ at CNP indicated by dash. Outside the immediate vicinity of CNP effective carrier mobilities μ estimated from $\rho_{xx} = \frac{1}{en_b\mu}$ in the Drude model are not much affected by the irradiation process, confirming that scattering events by Frenkel-pair point defects are scarce and the main effect is charge compensation. Shubnikov-de Haas (SdH) quantum oscillations of ΔR_{xx} and ΔR_{xy} in Bi_2Te_3 with magnetic field applied along the c -axis: **c**, before e -beam exposure, **d**, irradiated to a dose $89 \text{ C} \cdot \text{cm}^{-2}$ and **e**, to a dose $99 \text{ C} \cdot \text{cm}^{-2}$. The corresponding sizes of Fermi surfaces obtained from SdH (Supplementary Table 1) are cartooned as circles. **f**, **g**, **h**, Low-field R_{xy} for the samples in **c**, **d**, and **e**. The Fermi level (dashed line) is moving from the bulk valence band (BVB) in **(f)** to the bulk conduction band (BCB) in **(h)** as illustrated in insets by the cartoons of calculated⁵ Bi_2Te_3 band structure. **i**, The Landau level index plot *vs.* field minima in the SdH oscillations in **c** (red) and **d** (blue) yields an estimate of Berry phase $\varphi_B = 2\pi\beta$, see text. **j,k**, Cartoons of a TI with conducting bulk before irradiation (**j**) and after, with ideally only topological surfaces conducting (**k**).

Figure 3 | Time evolution of charge transport across charge neutrality point in

Bi_2Te_3 after ‘low-dose’ exposure. **a**, Evolution of longitudinal resistivity ρ_{xx} measured at 4.2 K after cycling to room temperature (RT) for a crystal irradiated with dose $\phi = 90 \text{ C} \cdot \text{cm}^{-2}$. Each RT dwell time is coded with a different color. Resistivity is seen to cross charge neutrality point (CNP) in reverse from n -type back to p -type. It is consistent with slow migration (hundreds of hours at RT) of vacancies (in accord with $\sim 0.8 \text{ eV}$ migration barriers, see text) and shows that CNP can be reached by designing a suitable thermal protocol. Insets show $\rho_{xx}(T)$ for n -type region (upper left) and p -type region (lower right). **b**, Change in mag-

netoconductance (MC) at different RT dwell times; here MC evolves from a quadratic field dependence of a typical bulk metal at short RT dwell times, through a complex region dominated by the charge-inhomogeneous bulk, to a weak antilocalization (WAL) region showing the characteristic low-field cusp near CNP. Here the data were normalized to the value at zero field. A fit to 2D localization theory²⁶ is shown as red line, see text.

Figure 4 | Stable charge neutrality point and 2D conductance in e-beam irradiated topological materials. **a**, Sheet resistance R_{xx} vs. temperature of Bi_2Te_3 crystal at the charge neutrality point (red line) exhibits a plateau at low temperatures - a thumbprint of 2D surface conduction, see right panels in **(e)** and **(f)**. We note that in Bi_2Te_3 , CNP and Dirac point do not coincide, with the Dirac point situated within a valley in the bulk valence bands⁵, and G_{xx}^{\min} is expected to reflect that²³. Magnetic field breaks time reversal symmetry and gaps Dirac bands, resulting in localizing behavior shown as dash. Inset: Optical image of the crystal showing van der Pauw contact configuration used. **b**, Annealing protocol with time steps $\Delta t = 30$ min implemented to tune Bi_2Te_3 crystal with dose $1 \text{ C} \cdot \text{cm}^{-2}$ back to stable CNP. Inset: Magnetoresistance at 1.9 K after each annealing step, with colors matched to indicate different annealing temperatures. **c,d**, ARPES spectra of a Bi_2Te_3 crystal irradiated with electron dose of $1.7 \text{ C} \cdot \text{cm}^{-2}$ taken along $\Gamma - K$ direction in the Brillouin zone. **c**, Prior to annealing the irradiated sample is n -type, with Dirac point at $E_{DP} \sim -290(10)$ meV relative to the Fermi level E_F . **d**, After annealing at 120°C Dirac point upshifts to a binding energy of $E_{DP} \sim -160(10)$ meV. The same shift is seen for the scans along $\Gamma - M$. **e**, WAL low-field quantum interference correction to the linear-in-field magnetotransport (**f**, also see text) at CNP in a Bi_2Te_3 crystal at 1.9 K with its characteristic low-field cusp. The 2D character of WAL is evident in its scaling with transverse field $H_\perp = H \cos \theta$, where θ is the tilt angle of the field measured from sample's c -axis. A fit to 2D localization (HLN) theory²⁶ (solid line) confirms that the contribution is only from two surfaces and yields a dephasing field $B_\phi = \frac{\hbar}{4el_\phi^2} \sim 0.01$ T. **f**, Linear magnetoresistance at CNP shows 2D scaling with H_\perp . **g**, WAL contribution at CNP in a $\text{Bi}_2\text{Se}_3:\text{Ca}(0.09\%)$ crystal at 1.9 K also scales with H_\perp . At high fields outside the cusp, the scaling is seen to fail for $\theta \gtrsim 60^\circ$. A fit to HLN theory (solid line) again confirms the contribution only from two surfaces and yields a smaller dephasing field $B_\phi \sim 0.004$ T (corresponding to dephasing length $l_\phi \sim 220$ nm). **h**, Linear magnetoresistance at CNP also scales with H_\perp .

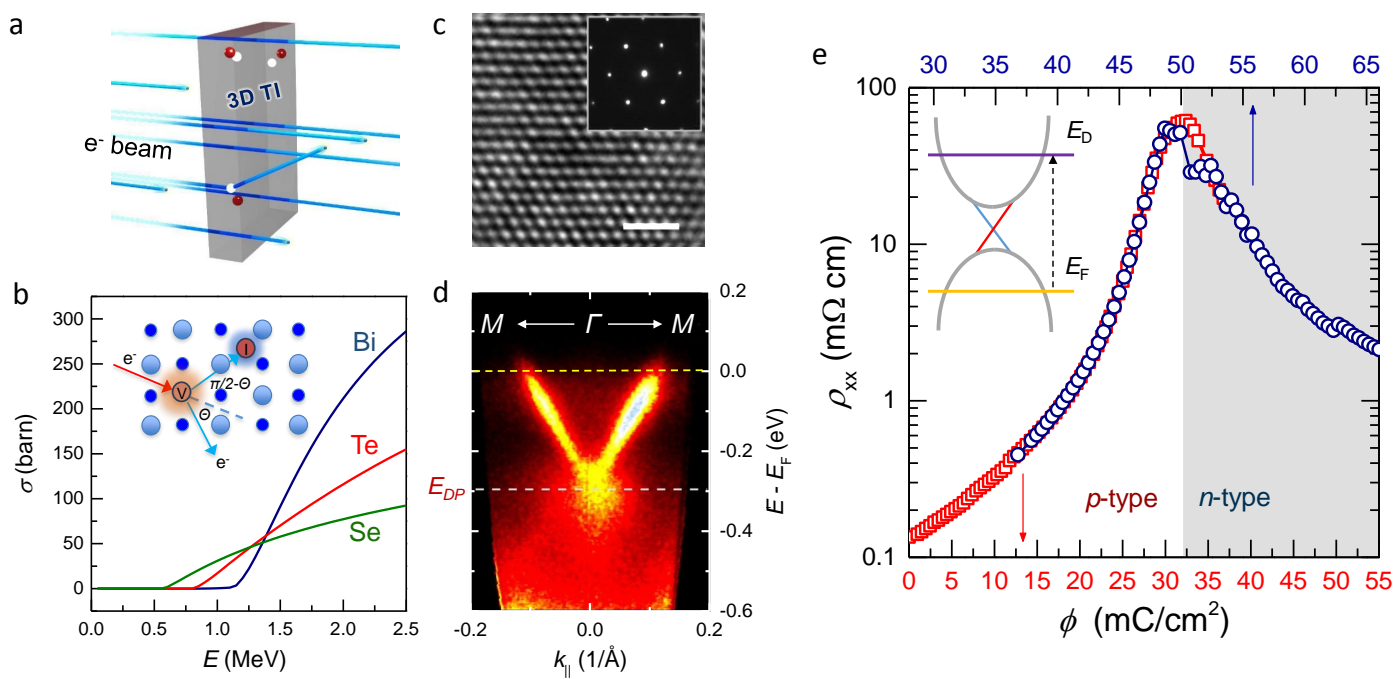


Fig. 1 irradi; ZZ *et al.*

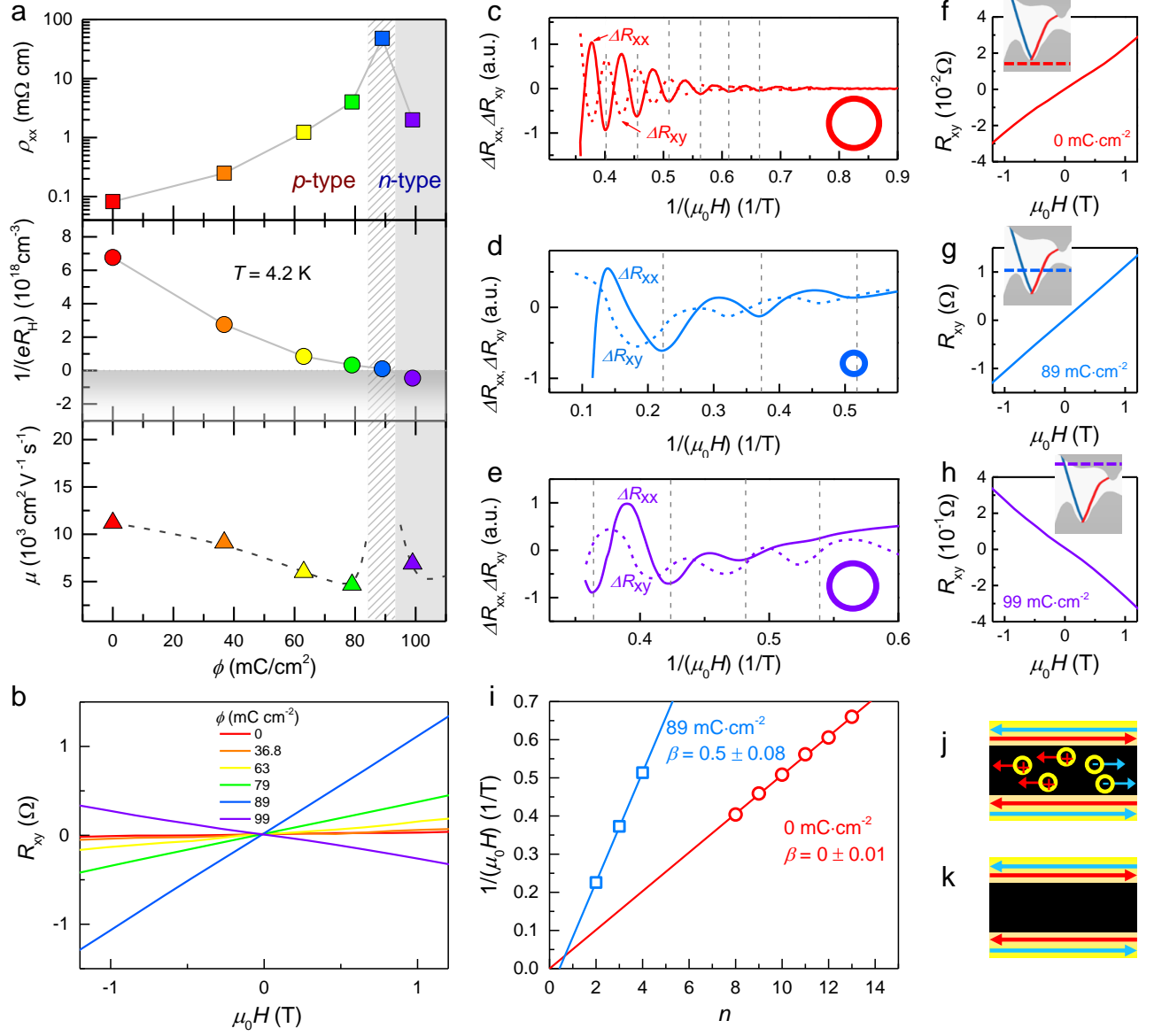


Fig. 2 irradi; ZZ *et al.*

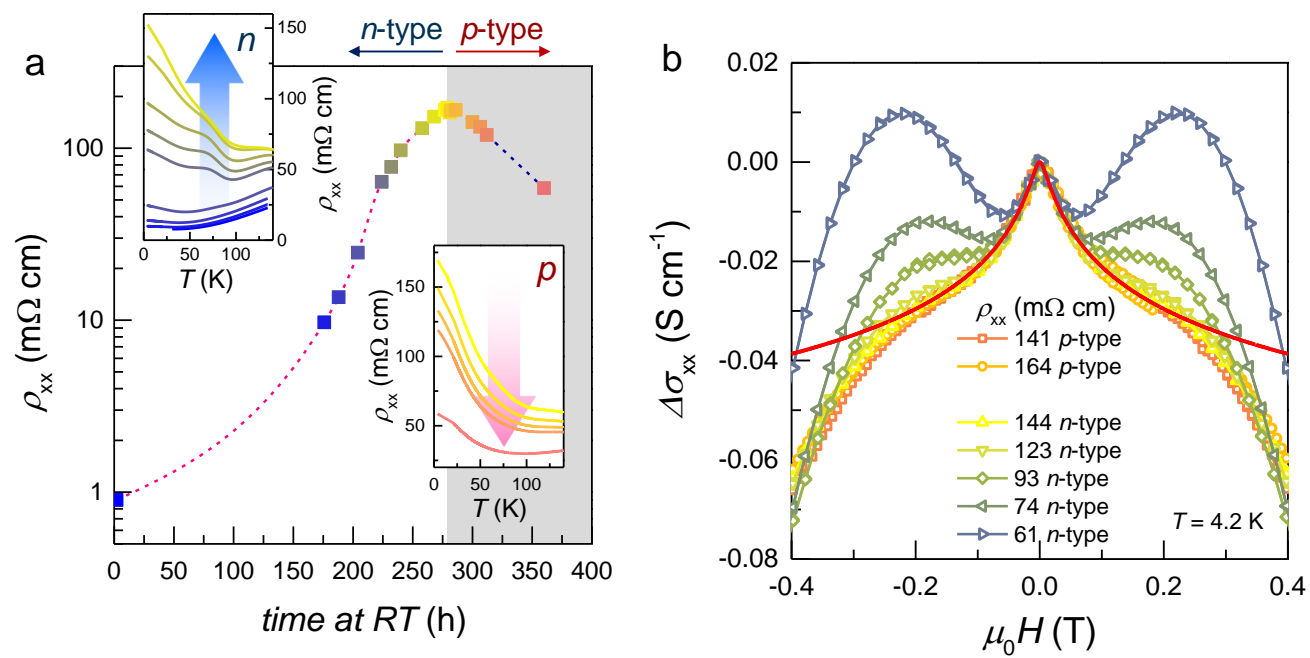


Fig. 3 irradi; ZZ *et al.*

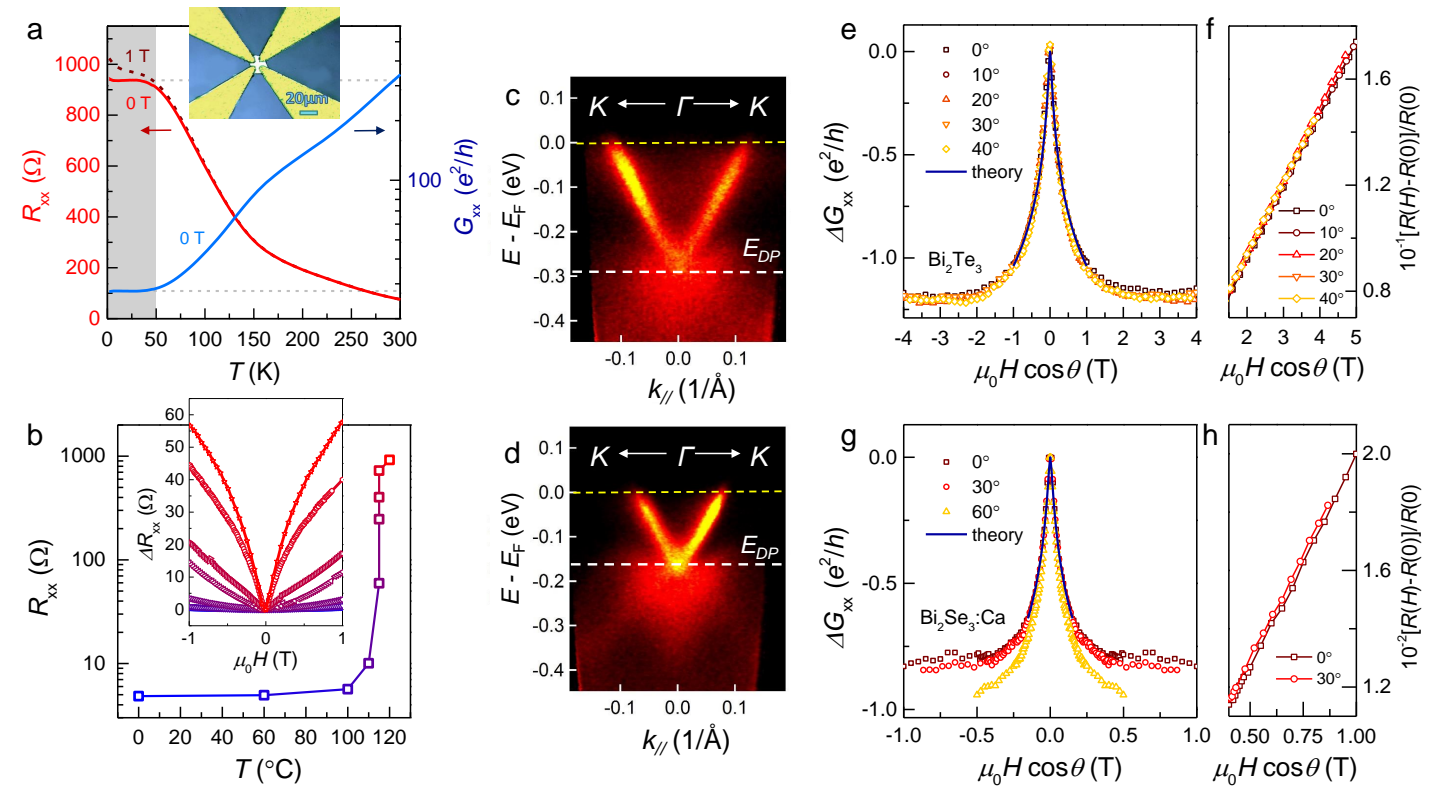


Fig. 4 irradi; ZZ *et al.*